

De Schryver, De Feyter, Schweizter (Eds.)  
Femtochemistry Wiley-VCH, Weinheim 2000

Submitted June 5, 2000

**Ultrafast probing and control of molecular dynamics:  
Beyond the pump-probe method**

Marcos Dantus

Department of Chemistry and Center for Fundamental Materials Research, Michigan State  
University, East Lansing, MI 48824, USA. Dantus@msu.edu

## **1. Introduction:**

The development of ultrafast laser pulses has outpaced the ability to create detectors with comparable time resolution for decades. This mismatch has necessitated the development of techniques based on two or more laser pulses with a time resolution that is limited only by the duration of the laser pulses themselves. The most common of these methods, capable of initiating a dynamic process and interrogating its time evolution, is known as pump-probe (PP). Probing can be achieved by monitoring absorption, LIF, ionization, multiphoton ionization, photoelectron detection, chemiluminescence and so forth. The pump probe method has been proven extremely powerful for the observation of ultrafast dynamics [1-4]. Each laser interaction involves the transfer of population, usually from the ground state to a state of interest by the pump and then to a second state by the probe. Because two populations are involved, the optical phase of the lasers is not important in these measurements [5,6].

Observation of the coherent interaction between the two laser pulses and the sample during a PP measurement requires phase locking and a detection system that filters out all the incoherent contributions. In order to harness the coherent properties in the observation and control of molecular dynamics laser setups that combine multiple laser beams coherently are preferred. Here we highlight four-wave mixing (FWM) methods for the observation and control of molecular dynamics in the gas phase. Four wave mixing involves three nonlinear electric field interactions to create a resulting fourth wave. Four-wave mixing methods can be considered analogous to pump-probe processes because they operate through the same order of nonlinearity. In the context of this chapter the first two interactions may induce a transfer of population while

the third one probes the dynamics of that state. When the FWM signal is heterodyned with an additional laser the analogy with PP is even more accurate [5,6].

We present on- and off-resonance experimental data to illustrate the power of FWM techniques. A semiclassical model is used to simulate the experimental results and to illustrate the mechanism for signal formation. Although FWM has been known for three decades and has been used to study solids, liquids and gases, we have focused on studying relatively simple and well-understood molecules in the gas phase in order to gain a deeper understanding of the FWM process itself. We present the observation of rotational and vibrational motion of ground state  $\text{HgI}_2$  using off-resonance impulsive excitation, as well as purely rotational motion for acetylene,  $\text{CO}_2$ ,  $\text{N}_2$  and pyroazine. For on resonance FWM, we contrast two types of nonlinear optical phenomena; photon echo and reverse transient grating. The former leads to the cancellation of inhomogeneous broadening in the sample, while the latter does not. A brief theoretical formulation is given to explain the mechanism for cancellation of inhomogeneous broadening for photon echo measurements. When carrying out FWM measurements with three time-ordered laser pulses, the pulse sequence can be used to control the nonlinear pathways that lead to signal observation. Here we illustrate this point by demonstrating coherent control over the observation of ground or excited state dynamics by changing the time between the first two pulses. Current and future applications of ultrafast four-wave mixing are also discussed.

## **2. Differences between the pump-probe method and four-wave mixing:**

This section analyses FWM techniques from the point of view of the PP method. For a thorough treatment of FWM methods the reader is referred to the texts of Mukamel and Boyd

[7,8]. FWM experiments are best understood using a density matrix approach. PP experiments, however, are usually represented by wave packet formalism in Hilbert space. Here we attempt to illustrate the different dynamics that can be addressed by the PP and FWM methods.

In a PP experiment, the first step involves a population transfer from the ground  $|g\rangle$  to the excited state  $|e\rangle$ . The probability  $P_{eg}$  for this process can be written quantum mechanically as follows,

$$P_{eg} = \left| \langle e | \mu E(t) | g \rangle \right|^2 = \langle e | \mu E(t) | g \rangle \langle g | \mu E(t)^* | e \rangle \quad (1)$$

where  $\mu$  is the induced dipole moment and  $E$  is the electric field. The probing step in a PP experiment involves the transfer of population from state  $|e\rangle$  to state  $|f\rangle$ . However, we must take into account that the population in state  $|e\rangle$  evolves in time. In a typical PP experiment one would monitor fluorescence resulting from the population in state  $|f\rangle$ . Coherent interactions between the laser pulses and off-resonance contributions occurring when pump and probe pulses overlap in time usually play a minimal role and are often neglected.

In contrast to PP, FWM methods are coherent spectroscopic techniques. That is, coherent interactions between the laser pulses account for most of the signal. The interaction between the lasers and the molecules takes place on a time scale that is much shorter than the fluorescence life time. For this reason, nonlinear optical methods are concerned with the transient polarization of the sample induced by the electromagnetic field. The FWM processes can be described in terms of the third order polarization resulting from the interaction with electromagnetic radiation.

$$P = P^{(0)} + P^{(1)} + P^{(2)} + P^{(3)} + \dots \quad (2)$$

where the total polarization is expanded to higher order terms [8: Shen, 1984 #59]. High order polarization can be achieved by a single intense laser pulse or by a series of less intense laser

pulses that interact coherently. The discussion here is restricted to the latter as it applies to isotropic media where even powers of the polarization vanish.

In order to distinguish between different FWM processes that contribute to the third order polarization one can take advantage of the wave vector properties of the laser pulses. Each laser pulse can be represented by the expression

$$E(\mathbf{r}, t) = E_0(t) \exp[-i(\omega t - \mathbf{k} \cdot \mathbf{r})] + E_0(t) \exp[i(\omega t - \mathbf{k} \cdot \mathbf{r})] \quad (3)$$

where  $E_0(t)$  is the time dependent envelope of the pulse,  $\omega$  is the carrier frequency,  $\mathbf{k}$  is the wave vector and  $\mathbf{r}$  is the sample spatial coordinate. If each laser has a different wave vector, that is, they are not collinear or they have different wavelengths, signals resulting from a particular combination of laser pulses can be isolated. This selection process is typically referred to as phase matching. Phase matching ensures conservation of energy and momentum for each nonlinear optical process. Here we will restrict the treatment to the case of three degenerate pulses where the detection geometry and pulse sequence is used to identify the different signals.

The phase matching condition restricts the sign of each electric field interaction, that is  $e^{i\omega t}$  or  $e^{-i\omega t}$ . The system, after a single resonant electric field interaction is left in a coherence state between the ground and the excited state. Two electric field interactions are required to create a population in the ground or the excited state. This is consistent with the linear dependence on laser intensity  $I \propto |E_0(t)|^2$ . These facts together with the requirement that electric field interactions occur coherently lead to most of the differences between PP and FWM measurements.

## 2.2 Off resonance FWM

For off-resonance laser interactions the polarization created by one electric field in the sample decays with a timescale that is shorter than most ultrafast laser pulses. When two laser

pulses are overlapped in time, however, a population can be obtained in the ground state. If the bandwidth of the lasers overlap several rotational and or vibrational states, the coherent superposition of states evolves as a function of time. The coherent superposition of vibrations and rotations in the ground state is probed by the third laser pulse which creates the third order polarization in the sample. The signal corresponds to the electric field that is emitted by the third order polarization in the sample [7]. Off resonance FWM is also known as transient grating spectroscopy[9]. The grating is formed in the sample by the crossing of the two plane-wave beams. Interference creates regions of high or low polarization in the sample. The third laser Bragg diffracts from the grating to generate the observed signal. The diffraction process is very similar to the diffraction of x-rays from crystalline systems because the spatial arrangement of the lasers leads to the *spatial coherence* in the sample.

The homodyne detected FWM signal intensity, resulting from the interaction between three incident laser pulses can be evaluated using

$$I_{FWM}(\tau) = \int_{-\infty}^{+\infty} |P^{(3)}(t)|^2 dt \quad (4)$$

where  $P^{(3)}(t)$  represents the time-dependent third-order polarization for a given phase matching condition. In the impulsive limit, when the laser pulse duration is negligible in comparison to the rotational and vibrational periods, FWM signal intensity simply reduces to

$$I_{FWM}(\tau) = |\chi^{(3)}(\tau)|^2 \quad (5)$$

where  $\chi^{(3)}(\tau)$  is the third order susceptibility associated with the molecular system. We can expand the susceptibility in terms of isotropic and anisotropic components  $\chi^{(3)}(t) = \chi_{\text{iso}}(\tau) + \chi_{\text{aniso}}(\tau)$  [10]

$$\chi_{iso}(t) = \langle \hat{i} [\alpha(t), \alpha(0)] \rangle \quad (6)$$

$$\chi_{aniso}(t) = \langle \hat{i} [\beta(t), \beta(0)] \rangle \langle C''(\theta(t)) \rangle \quad (7)$$

where  $[\cdot, \cdot]$  indicates commutator,  $\langle \cdot \rangle$  indicates quantum mechanical averaging,  $\alpha$  and  $\beta = (\alpha_{\parallel} + \alpha_{\perp})$  are the scalar and anisotropic part of polarizability respectively.  $C''(\theta(t))$  is the imaginary part of the correlation function of molecular orientation referenced to the angle  $\theta$  between the molecular axis and the laser's plane of polarization and is given by

$$C''(\theta(t)) = \frac{1}{k_B T} \frac{d}{dt} C(t), \quad (8)$$

where  $C(t)$  is the correlation function for molecular rotation[7].

## 2.3 On resonance FWM

On resonance excitation by a single electric field leads to a coherence that is much longer lived than that resulting from off-resonance excitation. According to Equation 1, the probability of population transfer from the ground to the excited state depends on two electric field interactions with the sample. In FWM, the lasers can be arranged such that each laser is responsible for a single field interaction. In such arrangements  $E(t)$  and  $E(t)^*$  can be manipulated independently. It is therefore possible to control the observed population transfer by changes in the optical phase or in the time delay between the first two pulses.

### 2.3.1 Controlling ground or excited state observation

The time delay between the first two pulses can be used to control the source of the FWM signal. This can be shown with a simple model that includes two vibrational levels in the ground state and two in the electronically excited state. For this reduced system (see Figure 1), it is possible to formulate the dynamics as a function of time delay between the first two pulses. The vibrational levels are separated by  $\hbar\omega_g$  and  $\hbar\omega_e$  in the ground and excited states respectively. The laser pulses are considered very short such that their bandwidth is larger than  $\omega_g$  or  $\omega_e$ . The three pulses are degenerate and resonant with the electronic transitions. The system is assumed to be at a temperature such that the two ground state levels are equally populated. After the first laser interaction the first order density matrix components depend on the sign of the electric field.

Interaction with  $e^{-i\omega t}$  yields

$$\rho_{eg}^{(1)} \propto \exp(-i\omega_{eg}t), \quad (9)$$

whereas, interaction with  $e^{i\omega t}$  yields

$$\rho_{ge}^{(1)} \propto \exp(i\omega_{eg}t), \quad (10)$$

The vibronic coherence formed by the first laser interaction involves the four vibrational levels from the two electronic states as shown in Figure 1. After one electric field interaction no population has been transferred, and this can be confirmed by the zeros in the diagonal elements of the first order density matrix in Figure 1.

Population transfer occurs upon interaction with the second laser pulse. The resulting expression contains the population of the four levels. Notice that populations (diagonal elements) are time independent. No relaxation has been included in our model. The simplified second order elements of the density matrix are given by populations

$$\rho_{gg}^{(2)} = -A \cos(\omega_e \tau_{12}/2), \quad \rho_{ee}^{(2)} = -A \cos(\omega_g \tau_{12}/2), \quad (11)$$

and vibrational coherences

$$\rho_{g'g}^{(2)} = -A \cos(\omega_e \tau_{12}/2) \exp(-i\omega_g t), \quad \rho_{ee'}^{(2)} = A \cos(\omega_g \tau_{12}/2) \exp(-i\omega_e t), \quad (12)$$

where the time delay between the two laser pulses is given by  $\tau_{12}$ , and  $A$  is a constant that depends on the laser intensity and transition dipole moment. The primes indicate different vibrational levels. The spatial dependence of the lasers has been omitted for clarity. Notice that the population and the vibrational coherence matrix elements have a term that depends on the time delay between the first two pulses. For certain values of this time delay one can cancel contributions from ground or excited state dynamics. The third electric field interaction generates the third order polarization given by the corresponding density matrix elements as shown in Figure 1.

### 2.3.2 Inhomogeneous broadening and photon echo measurements

Photon echo and spin echo are quite different phenomena. However, they have a large number of similarities. The Hahn spin echo [11] is illustrated in Figure 2 (top) . Notice that a coherent superposition of spins, originally pointed in the  $Z$  axis is rotated by 90 degrees into the  $XY$  plane. Inhomogeneous broadening in the sample causes dephasing of the coherent superposition as a function of time. Application of a 180 degree pulse causes an inversion in space and hence the spreading motion becomes a focusing motion that leads to a rephasing of the original superposition. This generates the spin echo. The process can also be carried out by separating the 180 degree pulse in to two 90 degree pulses. This setup is also known as Nuclear Overhauser Effect Spectroscopy (NOESY) [12].

The photon echo process involves different physics. The first interaction creates a coherent superposition of states (see Equation 9). Here the key is that the first pulse interacts with the *bra*, that is, the interaction is with  $e^{i\omega t}$ . All quantum mechanical states involved as well

as relaxation phenomena evolve with a positive sign. Subsequent  $e^{-i\omega t}$  interaction with two electric fields changes the sign of the evolution and the initial dephasing is reversed.

Here we give a brief description of the photon echo phenomena in terms of the model introduced in the previous section. The second order density matrix elements have an additional term that results from the spatial coherence in the sample. This term is described by

$$\rho_{grating}^{(2)} \propto \cos(\omega_{eg} \tau_{12}) = \{\exp(i\omega_{eg} \tau_{12}) + \exp(-i\omega_{eg} \tau_{12})\}/2. \quad (13)$$

The third order density matrix elements belonging to the phase matching geometry having the first electric field interaction with  $e^{i\omega t}$ , also known as action on the *bra*, only have the positive component of Equation 3. The third order density matrix associated with photon echo phenomena is

$$\rho_{PE}^{(3)} \propto \exp(i\omega_{eg} \tau_{12}) \exp(-i\omega_{eg}(t - \tau_{12})) \quad (14)$$

and achieves a maximum value when  $t = 2\tau_{12}$ . In section 4 we present an experimental demonstrations of this phenomenon.

### 3. Experimental methods:

Collinear laser geometry as used in most PP measurements is usually avoided for FWM. We have depicted diagrammatically the most common FWM laser configurations in Figure 3. The first setup shows two laser beams crossing at the sample, one beam interacts twice with the sample while the other one interacts only once. Two types of signals can be obtained. One with phase matching geometry  $\mathbf{k}_{PE} = -\mathbf{k}_1 + (\mathbf{k}_2 + \mathbf{k}_2)$  can be used to carry out photon echo measurements. The second coincides with the beam with wave vector  $\mathbf{k}_2$  and is given by  $\mathbf{k}_S = \pm (\mathbf{k}_1 - \mathbf{k}_1) + \mathbf{k}_2$ . This signal contains photon echo and virtual echo components [13]. It is possible

to use this arrangement with pairs of phase locked pulses in order to have better control over the pulse sequence and to heterodyne the signal.

The second laser arrangement in Figure 3 involves three distinct laser pulses in a plane crossing at the sample [14]. In this case the background free signal can be collected in two phase matching conditions. The virtual echo signal is collected at  $\mathbf{k}_{VE} = \mathbf{k}_1 - \mathbf{k}_2 + \mathbf{k}_3$  while the photon echo signal is collected at  $\mathbf{k}_{PE} = -\mathbf{k}_1 + \mathbf{k}_2 + \mathbf{k}_3$ . The two three-pulse signals can be used to determine the homogeneous and inhomogeneous relaxation rates of the sample using the same laser arrangement with two detectors.

The third laser arrangement in Figure 3 (bottom) is known as forward box geometry [15]. There are a number of advantages to the forward box geometry. First, virtual echo and photon echo measurements can be made with a single detector at the phase matching geometry. The beams can take any ordering and for this reason the beams have been labeled  $\mathbf{k}_a$ ,  $\mathbf{k}_b$  and  $\mathbf{k}_c$ . Second, the coherence is achieved spatially by the laser and it is not necessary to phase-lock the laser pulses. Third, for this arrangement there is no possibility of interference between the beams. Background free detection requires only one detector.

In the forward box configuration, the different nonlinear phenomena are determined by the pulse ordering. Here we show reverse transient grating RTG using  $\mathbf{k}_{RTG} = \mathbf{k}_c - (-\mathbf{k}_a + \mathbf{k}_b)$ , photon echo  $\mathbf{k}_{PE} = -\mathbf{k}_b + (\mathbf{k}_a + \mathbf{k}_c)$ , virtual echo  $\mathbf{k}_{VE} = \mathbf{k}_a - \mathbf{k}_b + \mathbf{k}_c$ , and stimulated pulse photon echo  $\mathbf{k}_{SPE} = -\mathbf{k}_b + \mathbf{k}_a + \mathbf{k}_c$ . The pulse ordering is written from left to right and time-overlapped pulses are indicated with a parenthesis. The observation of cascaded signal involving the free-induction decay emission from the one or more of the laser pulses is possible for the pulse sequence  $\mathbf{k}_{C-FID-FWM} = \mathbf{k}_a + \mathbf{k}_c - \mathbf{k}_b$  and is discussed elsewhere [16,17].

The experiments discussed here have been obtained with an amplified colliding-pulse mode-locked laser producing  $\sim 60$  fs transform limited pulses with  $0.3 \mu\text{J}$  of energy per pulse [18] The central wavelength of the pulses is  $620 \text{ nm}$ . This wavelength is important for resonant excitation of the B-X transition in molecular iodine [19].

Experiments are shown for two different samples. Off-resonance experiments are shown for  $\text{HgI}_2$ . The sample was sealed in a quartz cell evacuated to  $10^{-6}$  Torr. For the measurements, the cell was heated to  $280^\circ\text{C}$  to obtain a vapor pressure of approximately 100 Torr. The resonance measurements were carried out on molecular iodine. Iodine was also sealed in an evacuated quartz cell. Data was obtained as a function of temperature to demonstrate the temperature dependence of inhomogeneous and homogeneous broadening. Other samples were measured at room temperature.

#### **4. Results:**

In the PP method the signal measured the population transfer induced by the pump and probe lasers, while in the FWM method the signal arises from the laser induced polarizations in the sample. This fact leads to most of the differences between the two methods. In most PP experiments the signal arises from the population of molecules excited by the pump laser that absorbs the probe laser. FWM signal depends on the coherent mixing of the incident electric field and their enhancement by the sample.

##### **4.1 Off -resonance measurements:**

Here we illustrate the advantage of off-resonance FWM for the observation of ultrafast rotational and vibrational motion in ground states. The experimental data on gas phase  $\text{HgI}_2$

together with the theoretical simulation are shown in Figure 4. The transient consists of three contributions. At time zero there is a sharp feature corresponding to the isotropic instantaneous polarizability. This feature has no dependence on the intramolecular degrees of freedom and it is observed for all media including isolated atoms[20,21]. The data shows a fast vibration that is modulated by a very low frequency envelope. The vibrations with a 211 fs period correspond to the symmetric stretch, the only Raman active mode in this linear molecule [22]. The slow modulation belongs to the anisotropic contribution to the signal that depends on the molecular orientation.

Modeling of the data in Figure 4 requires us to define the isotropic and anisotropic contributions to the susceptibility. Only vibrational motion contributes to the isotropic susceptibility (Equation 6). Based on the bandwidth of our laser pulse only a few vibrational overtones are excited coherently. We approximate the isotropic susceptibility with

$$\chi_{iso}(t) = A_v \cos(\omega_v t + \phi_v) \quad (15)$$

where  $A_v$  is the relative amplitude of the vibrational contribution  $\omega_v$  is the frequency of the vibrational mode involved and  $\phi_v$  is the phase.

The anisotropic part of the susceptibility depends on the changes in orientation of the anisotropic molecules caused by rotational motion with some contribution from vibrational motion. For rotations, we can use a semiclassical approximation for the correlation function

$$C_J(t) = \cos(\omega_J t) \quad (16)$$

where the rotational frequency  $\omega_J$  depends on the Raman selection rules  $\Delta J = 0, \pm 2$  and is given by  $2\pi c[(4B)(J+3/2)]$ , where B rotational constants. Taking the derivative indicated in Equation 8 and performing the averaging over all rotational states indicated in Equation 7 we obtain

$$\langle C''(\theta(t)) \rangle \propto \sum_J n_J \omega_J \sin(\omega_J t) \quad (17)$$

where  $n_J$  is the thermal population of rotational states with different momentum  $J$ . For samples in thermal equilibrium we use a Boltzmann distribution for  $n_J$ . Joining both vibrational and rotational contributions we obtain the following expression for the anisotropic susceptibility

$$\chi_{aniso}(t) = A_r \cos(\frac{1}{2}\omega_v t + \phi_r) \sum_J n_J \omega_J \sin(\omega_J t). \quad (18)$$

where  $A_r$  is proportional to the anisotropic polarizability,  $\beta$ , and is inversely proportional to the temperature of the sample. There is an additional zero-time feature with amplitude  $A_z$  that arises from the equilibrium isotropic polarizability  $\alpha_0$ . The complete formula for our model is

$$\chi^{(3)}(t) = A_z(t) + A_v \cos(\frac{1}{2}\omega_v t + \phi_v) + A_r \cos(\frac{1}{2}\omega_v t + \phi_r) \sum_J n_J \omega_J \sin(\omega_J t) \quad (19)$$

Convolution of the simulation by the finite temporal width of our laser pulses yields the final results.

The simulation of the  $\text{HgI}_2$  data is shown in Figure 4 (line) together with the experimental data (dots). It is clear that the model reproduces the most salient characteristics of the data. The small differences between model and data could be reduced using a nonlinear least-squares fitting routine. In our model, only the three amplitude parameters have been adjusted, all the other values have been obtained from spectroscopic parameters [22,23].

## 4.2 Resonance measurements:

As discussed earlier for on-resonance FWM, the first laser pulse induces a polarization in the sample. Here we illustrate this process by contrasting reverse transient-grating (RTG) [21] and photon echo (PE) experiments. For these experiments the first laser pulse excites a polarization and after a variable time  $\tau$  the remaining two lasers, overlapped in time, probe the

polarization. The experiments are carried out in gas phase molecular iodine and the polarization involves a coherent superposition of electronic, vibrational and rotational states.

The data for the RTG and PE measurement is shown in Figure 5. The pulse sequence for RTG is  $E_c$  followed by  $E_b$  and  $E_a$  ( $\mathbf{k}_S = \mathbf{k}_1 + \mathbf{k}_2 - \mathbf{k}'_2$ ) while for PE it is beam  $E_b$  followed by beams  $E_a$  and  $E_c$  ( $\mathbf{k}_S = -\mathbf{k}_1 + \mathbf{k}_2 + \mathbf{k}'_2$ ). The differences observed in the background, undulation and apparent signal to noise in these data result from the difference in the first pulse interaction. As discussed in Section (2.3.2), when the first beam acts on the *bra*, the subsequent laser interactions lead to a cancellation of the inhomogeneous broadening in the sample and to the observation of the photon echo. When the first interaction occurs on the *ket*, there is no mechanism to cancel the inhomogeneous contributions to the signal. For gas phase molecules inhomogeneous contributions arise from differences in molecular speed ‘Doppler broadening’, as well as differences arising from the thermal distribution of initial rotational and vibrational states in the sample prior to laser excitation. The RTG data shows a strong background, a slow undulation that results from the inhomogeneous rotational population of the sample. After the first 3 ps, the RTG data shows a mixture of ground and excited state dynamics. The observation of ground state dynamics results from the initial thermal population of different vibrational modes. This inhomogeneity is observed as vibrational ‘hot bands’ in this time domain spectrum. In the PE data, only excited state vibrational dynamics are observed.

The cancellation of inhomogeneous broadening in PE measurements has been recognized since the first photon echo measurement in 1964 [24,25]. This advantage has been exploited for example to measure the homogeneous lifetime of complex systems such as large organic molecules in solution [26-28]. Here we illustrate how this method works for molecular iodine. In Figure 6, we present RTG and PE measurements for molecular iodine taken with long time

delays. The measurements are taken as a function of temperature to illustrate the different mechanisms for coherence relaxation. Notice that the RTG measurements appear not to be temperature dependent in this temperature range (see Fig. 6a). The reason for this observation is that the inhomogeneous contributions are overwhelming the homogeneous relaxation. In the PE measurements, we can see that the homogeneous relaxation times are much longer and are found to decrease with temperature. The cause for the decreased coherence lifetime is an increase in the number density and hence an increase in the collision frequency.

### **4.3 Coherent control with FWM**

The coherent nature of FWM experiments provides the opportunity to harness the coherent properties of lasers for controlling intra- and inter-molecular degrees of freedom. We have been exploring FWM methods in our group to achieve coherent control of molecular dynamics [18,29,30]. Here we illustrate this work with one such example. The data in Figure 7 was obtained with molecular iodine. The time delay between the first two pulses was controlled to be 614 fs (upper transient) or 460 fs (lower transient). The upper transient shows mostly ground state vibrations with a 160 fs period. The lower transient shows exclusively excited state vibrations with a period of 307 fs.

The mechanisms for signal formation are illustrated in the inserts using ladder diagrams. For the upper transient the process can be understood in terms of coherent Raman scattering process. The second pulse creates a coherent superposition of vibrational states in the ground state. This process is enhanced when the time between the first and second pulses matches the vibrational period of the excited state [18,29]. The third laser pulse probes the resulting ground state vibrational coherence. For the lower transient the time delay between the first two pulses

does not permit the transfer of the excited state superposition of states to the ground state. In this case, signal formation occurs by excitation of a new-excited state superposition by pulse  $E_b$  shown with gray arrows. Probing with pulse  $E_c$  results into observation of excited state dynamics. The model described in Section (2.3.1) can be used to explain these results more rigorously. These results show one of the several coherent manipulations that are possible using FWM.

## 5. Discussion:

### 5.1 Off-resonance FWM and time-resolved measurements of ground state dynamics

Off resonance FWM, is analogous to coherent Raman scattering, and like its spectrally resolved cousins provides ground state spectroscopic information. Here we have demonstrated the observation of vibrational and rotational motion of ground state  $\text{HgI}_2$ . Elsewhere other groups as well as our group have shown that with this method it is easy to observe rotational coherence from gas phase ensembles of molecules [21,31-33]. Observation of rotational revivals for time delays of 100 ps with a time resolution of 10 fs allows the determination of rotational constants with a  $10^{-5} \text{ cm}^{-1}$  resolution [21,34]. With additional care  $10^{-6} \text{ cm}^{-1}$  accuracy is possible. This level of accuracy is already in the range of some high-resolution frequency resolved methods. Time resolved rotational coherence has been pursued for the determination of complex molecular systems in the gas phase [34]. Femtosecond time resolution allows work on lighter molecules such as  $\text{D}_2$  [35] and work at high temperatures.

Off-resonance experiments can be used to measure molecular dynamics in gas mixtures. In Figure 8 we illustrate the types of experiments that are possible. The experimental data show only the early time rotational dynamics from three different samples, acetylene, car exhaust and

pyrazine. The time at which the first feature reaches its maximum can be used to extract the rotational constant, albeit with less accuracy than for a full recurrence. For acetylene and for pyrazine we find 1.8 and 0.21  $\text{cm}^{-1}$  respectively. These values are in good agreement with the published rotational constants [36]. The data on the car exhaust sample obtained at room temperature demonstrates the ability of off-resonance FWM for analyzing mixtures of compounds and products of chemical reactions. The initial dephasing feature has been deconvoluted as a sum of three components. The first feature due to the instantaneous polarizability at time zero, the second due to nitrogen and the third to carbon dioxide. Measurement of the rotational recurrences directly results in much higher accuracy as discussed earlier [21]. At present, we are pursuing different applications of off-resonance FWM for the study of chemical reactivity.

## **5.2 Resonance FWM, ground and excited state dynamics**

Resonance FWM allows the coherent excitation of ground as well as excited state dynamics. Here we have presented results obtained from molecular iodine in the gas phase. The goal of these experiments has been to illustrate the possibilities afforded by coherent spectroscopic methods such as FWM. We have shown how using a specific laser configuration the sign of the electric field interactions can be regulated. This control leads to photon echo type of measurements that cancel inhomogeneous contributions to the signal. Although the photon echo phenomenon has been known for over two decades, we find it valuable to demonstrate the process experimentally in a well-understood sample. We have included a simple formulation that is independent of molecular complexity. The reverse transient grating measurements have been contrasted to show the effect of inhomogeneities in the sample.

Resonant FWM experiments have other advantages over PP methods. In FWM, the dynamics depend on the ground or the excited states. In the PP method, the dynamics depend on the population transfer from the ground to the excited state and on the time-dependent transition probability between that state and a second excited state. This second transition is not always well-known because potential energy surfaces are not easily determined. Interpretation of the PP data depends on assumptions about the spectroscopic probe transition. In FWM measurements, the ground state can be obtained from off-resonant measurements leaving only the first excited state to be determined. This should make these methods more powerful for inverting the time domain data for constructing the potential energy surfaces than PP methods.

Our experiments demonstrate the use of a time delay to enhance the FWM signal from the ground state. These experiments can be understood in terms of coherent anti-Stokes Raman scattering (CARS). With tunable femtosecond lasers it is possible to deposit any amount of excess energy in the ground state and to follow the ensuing dynamics. Zewail and co-workers used degenerate FWM for probing real time reaction dynamics [37]. Femtosecond CARS experiments have been carried out by Hyden and Chandler [38], Materny [39,40] and Prior [41].

It is well known that multiphoton transitions are easily achieved with ultrafast pulses. In fact, it is sometimes extremely difficult to observe single photon transitions in certain molecular systems. Using FWM, one can determine the phase matching geometry based on the type of process that one wants to observe. Detection at that geometry provides a mechanism to filter out all other processes and to count the number of photons involved in the laser-molecule interactions.

When the FWM signal is time gated, a second dimension is uncovered that identifies the nature of the coherent superposition of states that leads to signal formation. This information can

also be obtained by spectrally dispersing the FWM signal [30,42]. The additional information allows the elucidation of dynamics processes that are masked in one dimensional techniques. The two-dimensional information obtained in this measurement promises to unravel the mechanisms for energy transfer in complex liquid systems [7]. We have used this method to determine the role of chirp in laser excitation. Efforts on six-wave mixing are currently underway in various laboratories [43-47].

In our group, we are continuing our efforts to use FWM methods as a convenient way to coherently combine three laser pulses. We have explored different pulse sequences to control the different Liouville pathways that lead to signal formation [17]. The long coherence lifetimes of gas phase molecules provide the opportunity for designing arrangements where multiple coherent interactions are possible. Such setups should be of interest for the coherent manipulation of large numbers of quantum mechanical states. Currently, we are working on the extension of these methods to the ultraviolet wavelength in order to interrogate chemical reactions.

## **6. Acknowledgements:**

The research presented here is the result of the hard work and dedication of Igor Pastirk, Emily J. Brown, Dr. Vadim V. Lozovoy and Dr. Bruna I. Grimberg in the Dantus Laboratory. Support of this work from the National Science Foundation Grant CHE-9812584 is gratefully acknowledged. Additional funding comes from a Packard Science and Engineering Fellowship, an Alfred P. Sloan Research Fellowship and a Camille Dreyfus Teacher-Scholar award.

## FIGURE CAPTIONS

Fig. 1, Energy diagram showing two electronic states with two vibrational levels each. The density matrix is given before electric field interaction  $\rho^{(0)}$ , after one  $\rho^{(1)}$  and two electric field interactions  $\rho^{(2)}$ . The diagonal terms correspond to the populations. The initial state has an equal population of levels 1 and 2. The off diagonal elements in  $\rho^{(1)}$  correspond to vibronic coherences while those in  $\rho^{(2)}$  correspond to vibrational coherences.

Fig.2, (Top) Schematic representation of the Hahn spin echo used in nuclear magnetic resonance. The diagrams indicate the pulse sequence as well as a representation of the spin in spatial coordinates. The second pulse sequence corresponds to Nuclear Overhauser Effect Spectroscopy. (Bottom) Schematic representation of the photon echo phenomena. Notice the similarity with the Hahn spin echo pulse sequence. The first electric field interaction creates a coherence represented here by the first order density matrix elements  $\rho_{ge}^{(1)}$  with evolution on the *bra*, after two more electric field interactions the third order density matrix elements  $\rho_{eg}^{(3)}$  evolve on the *ket*. The photon echo is strongest after a time equal to the time delay between the first two pulses. The second optical pulse sequence corresponds to the stimulated photon echo phenomena that is analogous with the NOESY sequence used in nuclear magnetic resonance.

Fig. 3, Experimental setups for FWM. (Top) Two-pulse setup. There are two possible phase matching directions where signal can be detected. The signal that coincides with  $\mathbf{k}_2$  contains photon echo and virtual echo components. The  $\mathbf{k}_{PE}$  direction can be detected background free. Notice that this setup is symmetric and a similar signal can be expected on the opposite side of  $\mathbf{k}_1$ . (Middle) Three-pulse setup. This setup allows the simultaneous collection of background free

virtual echo signal at  $\mathbf{k}_{VE}$  and photon echo signal at  $\mathbf{k}_{PE}$ . (Bottom) Forward box geometry. This setup allows background free detection of virtual echo and photon echo signal at  $\mathbf{k}_{VE}$ , the nature of the signal depends on the pulse sequence (see text).

Fig. 4, Off-resonance FWM signal obtained for gas-phase  $\text{HgI}_2$  as a function of time delay between the first two pulses and the third. The data shows a sharp response at time zero due to the instantaneous polarizability. The fast, 211 fs modulation corresponds to the coherent symmetric stretch vibration. The slow picosecond modulation corresponds to the rotational dynamics of the sample. The experimental data are shown as points, the theoretical simulation according is shown as a continuous line.

Fig. 5, Comparison between (a) reverse transient grating (RTG) and (b) photon echo (PE) signals for molecular iodine. The two scans were taken under identical condition except for the pulse sequence (see text). The RTG transient shows a large background, a slow modulation due to rotational dynamics and a mixture of ground and excited state vibrations. The PE transient shows only excited state vibrational motion.

Fig. 6, (a) Reverse transient grating signal for molecular iodine obtained for long time delays. The data was taken as a function of sample temperature. The average decay time measured is  $150 \pm 20$  ps. Notice that the RTG data show very little temperature dependence because dephasing is overwhelmed by inhomogeneous broadening in this temperature range. (b) Photon echo signal obtained under the same conditions as the RTG data. Notice that the PE transients do show marked temperature dependence, and this reflects the homogeneous relaxation, which depends

on sample density. The measured coherence relaxation times are  $390 \pm 17$ ,  $204 \pm 9$  and  $168 \pm 10$  ps for 88, 98 and 108 °C respectively.

Fig. 7, Virtual echo measurements on molecular iodine obtained for two different time delays between the first two pulses. (a) When the time delay between the first two pulses is 614 fs, ground state vibrational motion is observed. (b) When the time delay between the first two pulses is 460 fs, excited state vibrational motion is observed. The two transients were obtained as a function of time delay between the second and third pulses under otherwise identical conditions. The ladder diagrams indicate the nonlinear pathway responsible for signal formation, black arrows indicate action on the ket, gray arrows indicate action on the bra.

Fig. 8, Off-resonance FWM signals for different compounds. (Top) Initial rotational dynamics observed for gas phase acetylene molecules. (Middle) Initial rotational dynamics observed from a sample collected from car exhaust. The two main components are nitrogen and carbon dioxide. (Bottom) Initial rotational dynamics observed for gas phase pyrazine.

## References

- (1) *Femtochemistry*; Zewail, A. H., Ed.; World Scientific: Singapore, 1994; Vol. I and II.
- (2) *Femtosecond Chemistry*; Manz, J.; Wöste, L., Eds.; VCH: Weinheim, 1995; Vol. I and II.
- (3) *Femtochemistry: Ultrafast Chemical and Physical Processes in Molecular Systems*; Chergui, M., Ed.; World Scientific: Singapore, 1996.
- (4) *Femtochemistry and Femtobiology*; Sundström, V., Ed.; World Scientific: Singapore, 1998.
- (5) Fried, L. E.; Mukamel, S. *J. Chem. Phys.* **1990**, *93*, 3063-3071.
- (6) Tanimura, Y.; Mukamel, S. *J. Chem. Phys.* **1995**, *103*, 1981-1984.
- (7) Mukamel, S. *Principles of Nonlinear Optical Spectroscopy*; Oxford University Press: New York, 1995.
- (8) Boyd, R. W. *Nonlinear Optics*; Academic Press: San Diego, 1992.
- (9) Fayer, M. D. *Annu. Rev. Phys. Chem.* **1982**, *33*, 63.
- (10) Cho, M.; Du, M.; Scherer, N. F.; Fleming, G. R. *J. Chem. Phys.* **1993**, *99*, 2410.
- (11) Hahn, E. L. *Phys. Rev.* **1950**, *80*, 580.
- (12) Ernst, R. R.; Bodenhausen, G.; Wokaum, A. *Principles of nuclear magnetic resonance in one and two dimensions*; Oxford University Press: New York, 1987; Vol. 14.
- (13) Pshenichnikov, M. S.; de Boeij, W. P.; Wiersma, D. A. *Phys. Rev. Lett.* **1996**, *76*, 4701.
- (14) Weiner, A. M.; Silvestri, S. D.; Ippen, E. P. *J. Opt. Soc. Am. B* **1985**, *2*, 654.
- (15) Prior, Y. *Appl. Opt.* **1980**, *19*, 1741.
- (16) Lozovoy, V. V.; Pastirk, I.; Dantus, M. *Phys. Rev. Lett.* , (submitted).
- (17) Lozovoy, V. V.; Pastirk, I.; Brown, E. J.; Grimberg, B. I.; Dantus, M. *J. Chem. Phys.* **2000**, (submitted).
- (18) Pastirk, I.; Brown, E. J.; Grimberg, B. I.; Lozovoy, V. V.; Dantus, M. *Faraday Discuss.* **1999**, *113*, 401-424.
- (19) Tellinghuisen, J. J. *Quant. Spectrosc. Radiat. Transfer* **1978**, *19*, 149.
- (20) Shen, Y. R. *The Principle of Nonlinear Optics*; Wiley: New York, 1984.
- (21) Brown, E. J.; Zhang, Q.; Dantus, M. *J. Chem. Phys.* **1999**, *110*, 5772.

- (22) Clark, R. J. H.; Rippon, D. M. *J. Chem. Soc, Faraday Trans. 2* **1973**, *69*, 1496.
- (23) Spiridonov, V. P.; Gershikov, A. G.; Butayev, B. S. *J. Mol. Struct.* **1979**, *52*, 53.
- (24) Kurnit, N. A.; Abella, I. D.; Hartmann, S. R. *Phys. Rev. Lett.* **1964**, *13*, 567-570.
- (25) Patel, C. K. N.; Slusher, R. E. *Phys. Rev. Lett.* **1968**, *20*, 1087-1089.
- (26) Fleming, G. R.; Cho, M. H. *Ann. Rev. Phys. Chem.* **1996**, *47*, 109.
- (27) Vohringer, P.; Arnett, D. C.; Yang, T. S.; Scherer, N. F. *Chem. Phys. Lett.* **1995**, *237*, 387.
- (28) de Boeij, W. P.; Pshenichnikov, M. S.; Wiersma, D. A. *Annu. Rev. Phys. Chem.* **1998**, *49*, 99-123.
- (29) Brown, E. J.; Pastirk, I.; Grimberg, B. I.; Lozovoy, V. V.; Dantus, M. *J. Chem. Phys.* **1999**, *111*, 3779-3782.
- (30) Lozovoy, V. V.; Grimberg, B. I.; Brown, E. J.; Pastirk, I.; Dantus, M. *J. Raman Spectrosc.* **2000**, *31*, 41-49.
- (31) Heritage, J. P.; Gustafson, T. K.; Lin, C. H. *Phys. Rev. Lett.* **1975**, *34*, 1299.
- (32) Frey, H. M.; Beaud, P.; Gerber, T.; Mischler, B.; Radi, P. P.; Tzannis, A. P. *Appl. Phys. B* **1999**, *68*, 735-739.
- (33) Lavorel, B.; FAucher, O.; Morgen, M.; Chaux, R. *J. of Raman Spec.* **2000**, *31*, 77-83.
- (34) Hattig, C.; Hess, B. A. *J. Phys. Chem* **1996**, *100*, 6243.
- (35) Sarkisov, O. M.; Tovbin, D. G.; Lozovoy, V. V.; Gostev, F. E.; Autipin, A. A.; Umanskii, S. Y. *Chem. Phys. Lett.* **1999**, *303*, 458-466.
- (36) Herzberg, G. *Molecular Spectra and Molecular Structure*; Krieger Publishing Company: Florida, 1991; Vol. III.
- (37) Motzkus, M.; Pedersen, S.; Zewail, A. H. *J. Phys. Chem.* **1996**, *100*, 5620-5633.
- (38) Hayden, C. C.; Chandler, D. W. *J. Chem. Phys.* **1995**, *103*, 10465-10472.
- (39) Schmitt, M.; Knopp, G.; Materny, A.; Kiefer, W. *Chem. Phys. Lett.* **1997**, *280*, 339-347.
- (40) Schmitt, M.; Knopp, G.; Materny, A.; Kiefer, W. *Chem. Phys. Lett.* **1997**, *270*, 9-15.
- (41) Knopp, G.; Pinkas, I.; Prior, Y. *J. Raman Spectrosc.* **2000**, *31*, 51-58.

- (42) Pastirk, I.; Lozovoy, V. V.; Grimberg, B. I.; Brown, E. J.; Dantus, M. *J. Phys. Chem. A* **1999**, *103*, 10226-10236.
- (43) Tominaga, K.; Keogh, G. P.; Naitoh, Y.; Yoshihara, K. *J. Raman Spec.* **1995**, *26*, 495-501.
- (44) Tokmakoff, A.; Lang, M. J.; Larsen, D. S.; Chernyak, V.; Mukamel, S. *CHEM PHYS LETT* **1997**, *272*, 48-54.
- (45) Kirkwood, J. C.; Albrecht, A. C. *J. Raman Spec.* **2000**, *31*, 107-124.
- (46) Blank, D. A.; Kaufman, L. J.; Fleming, G. R. *J. Chem. Phys.* **1999**, *111*, 3105-3114.
- (47) Zhao, W.; Wright, J. C. *Phys. Rev. Lett.* **2000**, *84*, 1411-1414.

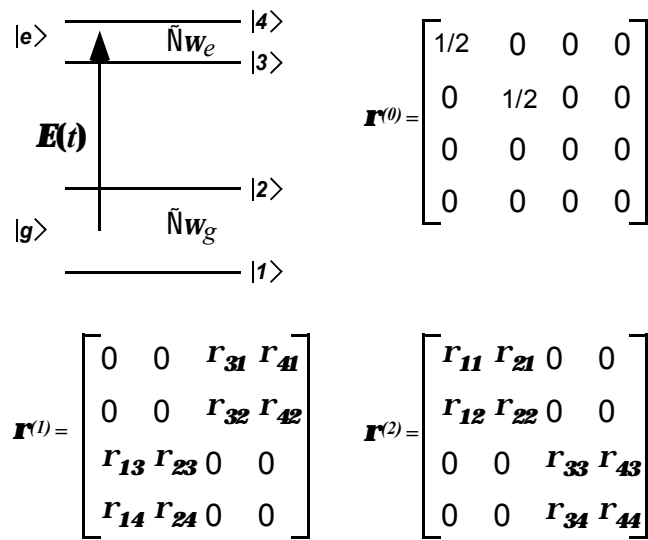
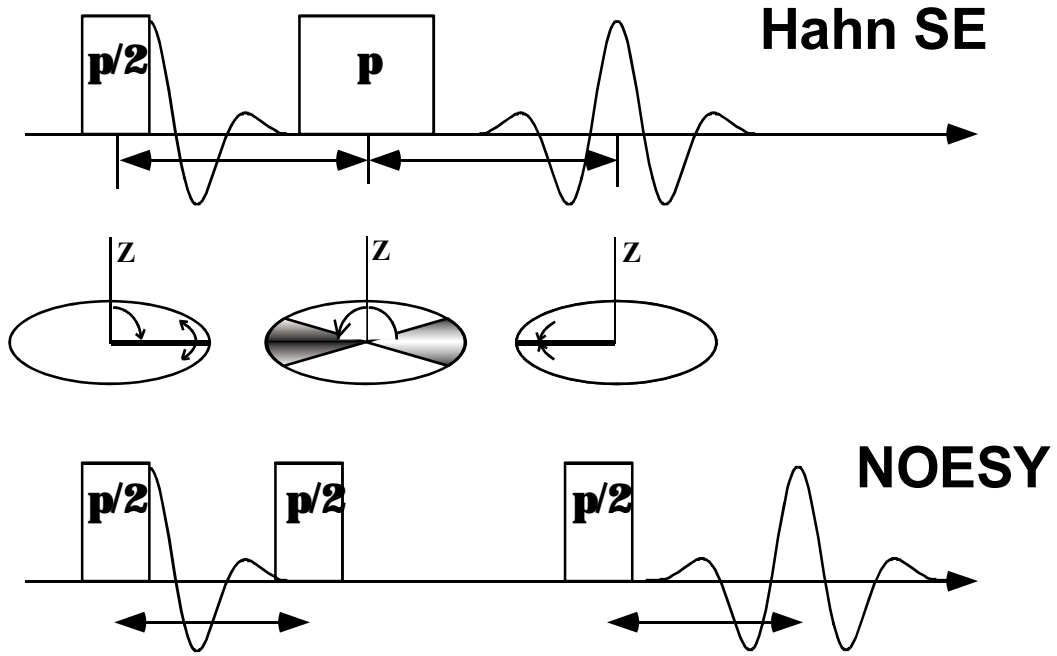
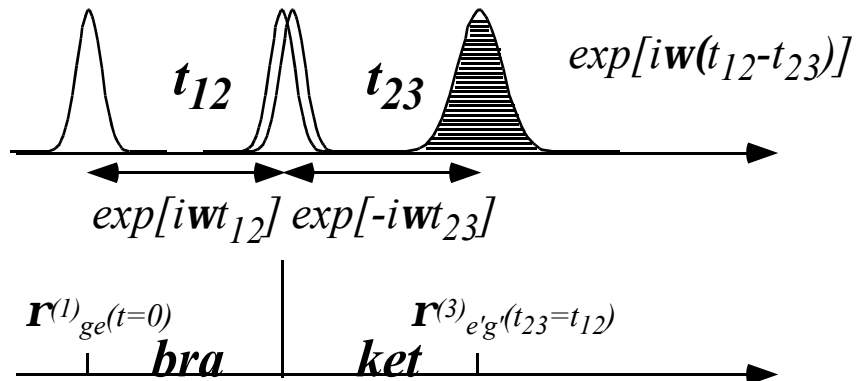


Fig. 1; Dantus, Femtochemistry

# Spin Echo



# Photon Echo



# Stimulated PE

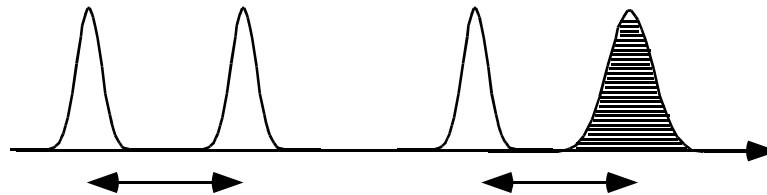


Fig. 2, Dantus, Femtochemistry

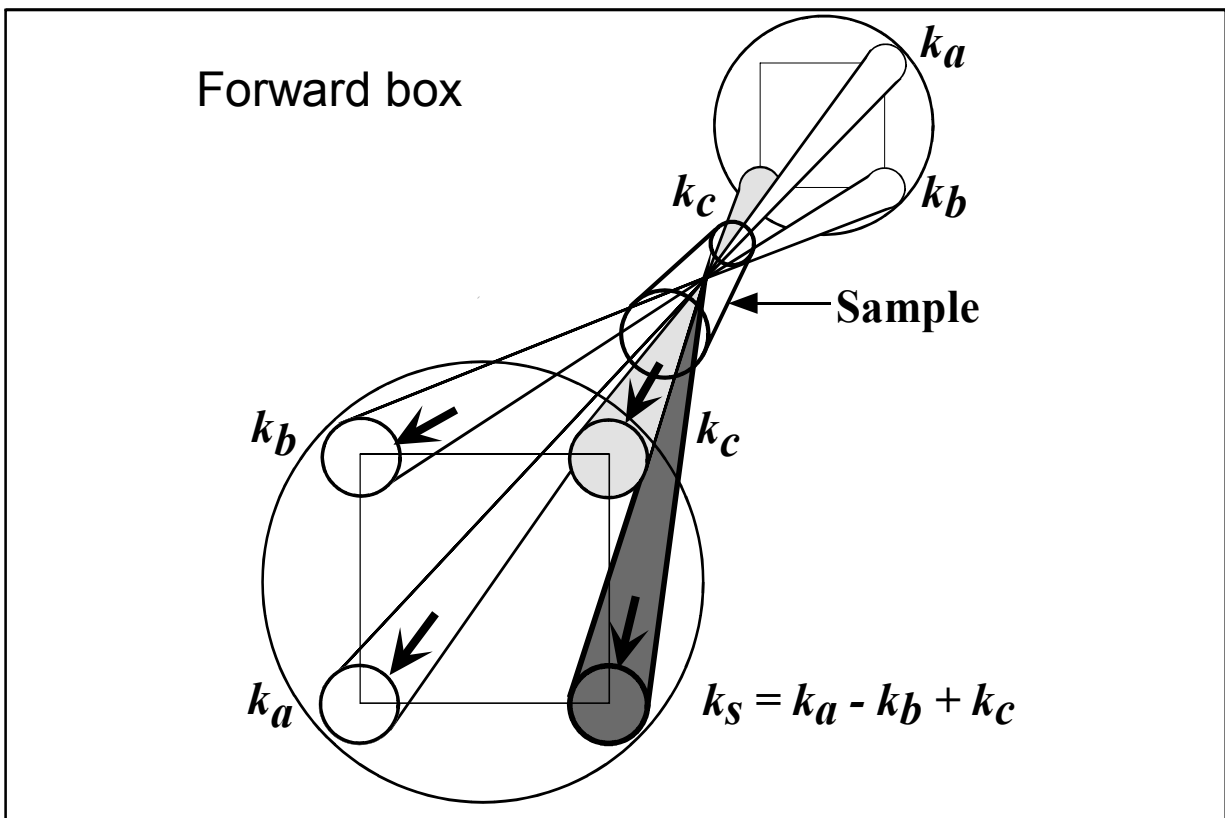
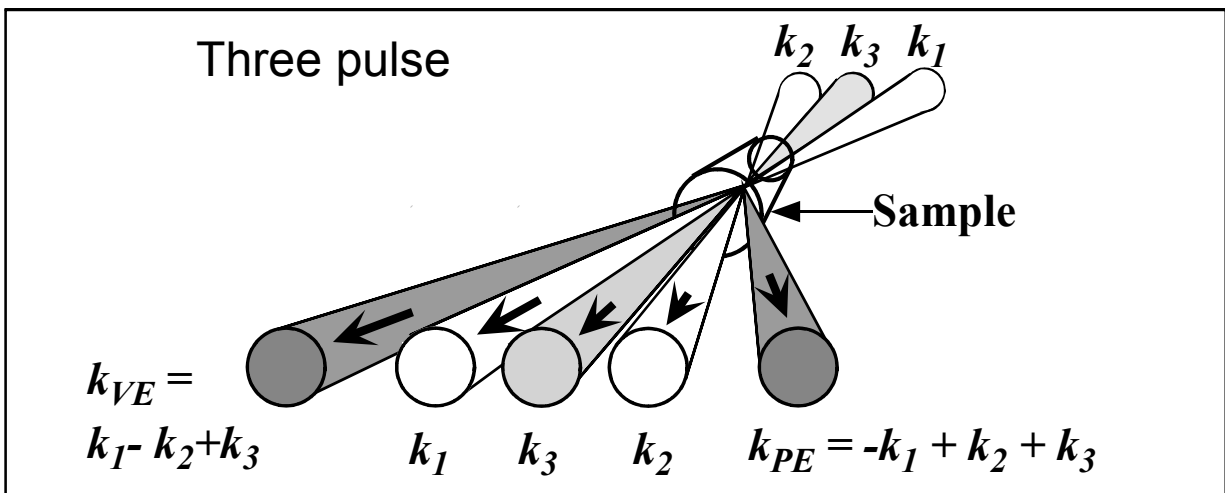
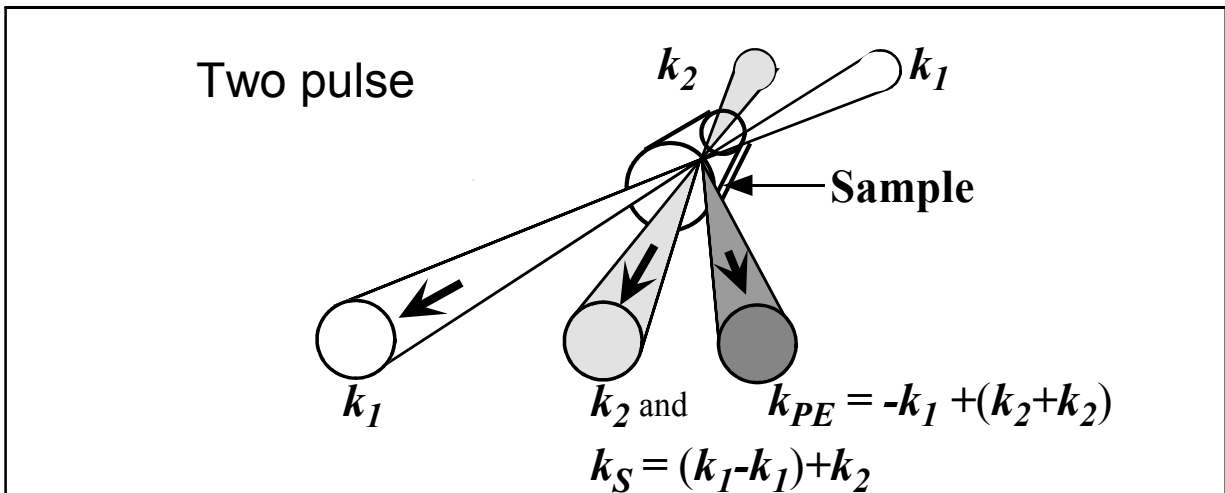


Fig. 3: Dantus. Femtochemistry

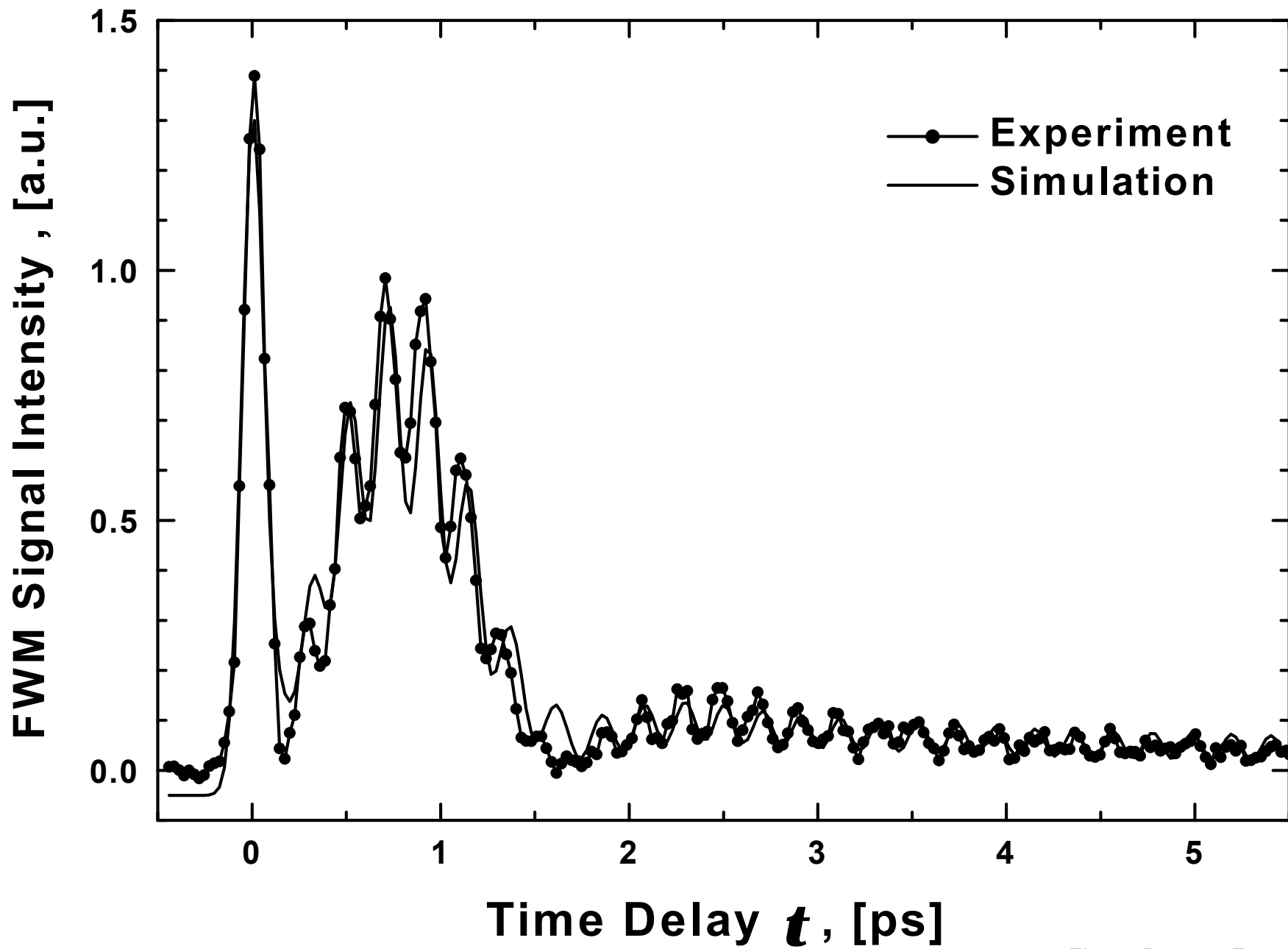


Fig. 4; Dantus, Femtochemistry

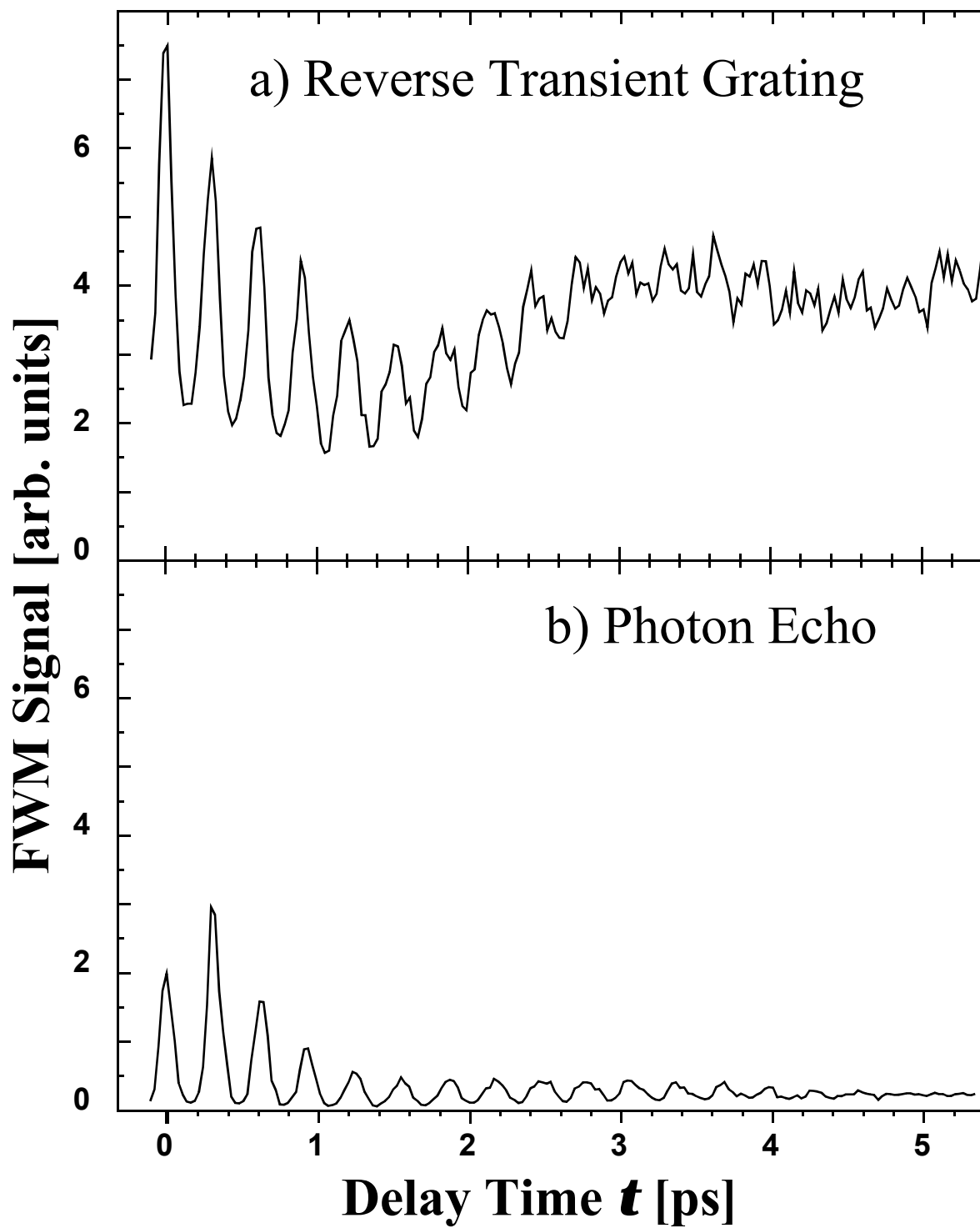


Fig. 5; Dantus, Femtochemistry

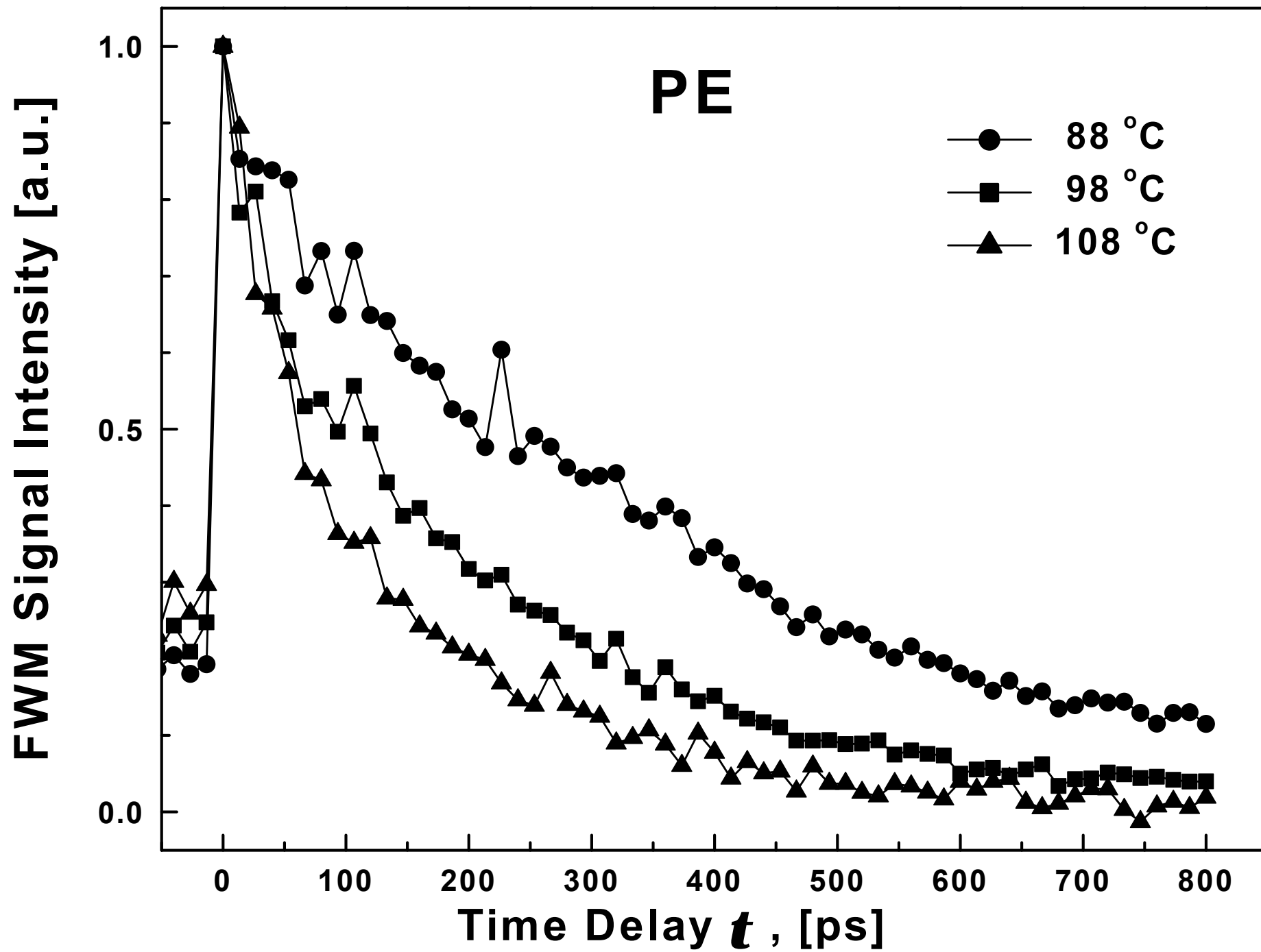


Fig. 6a; Dantus, Femtochemistry

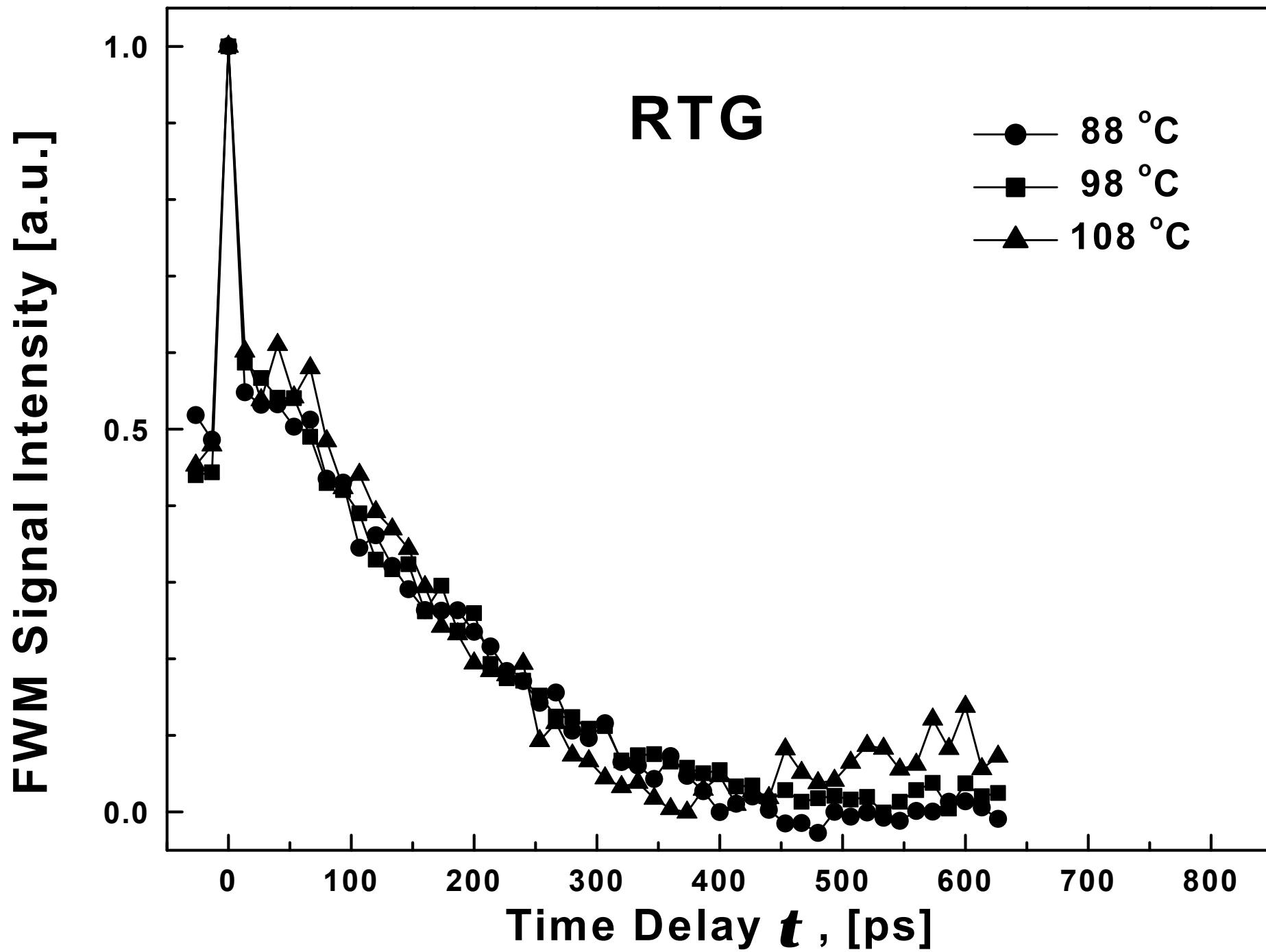


Fig. 6b; Dantus, Femtochemistry

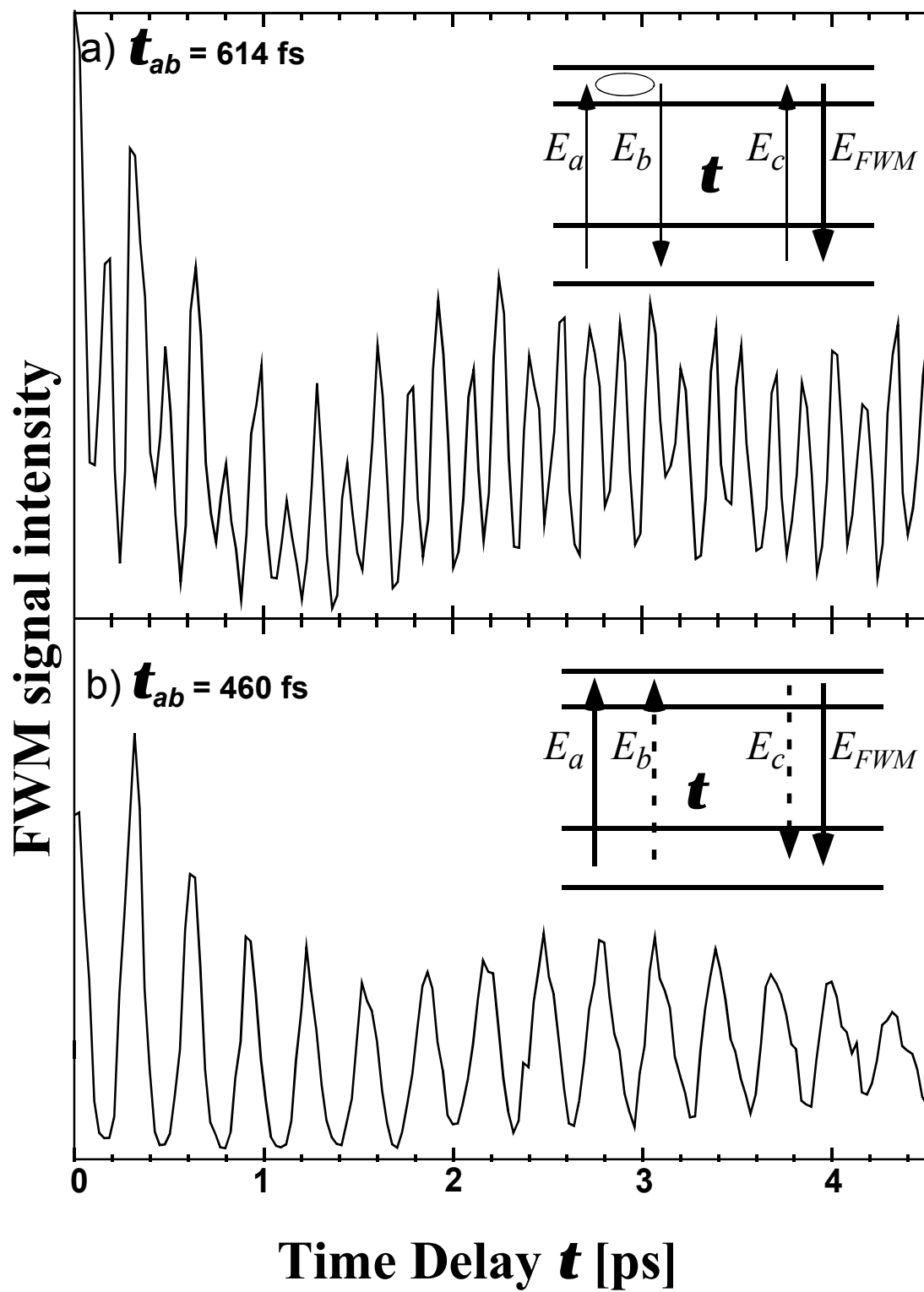


Fig. 7; Dantus, Femtochemistry

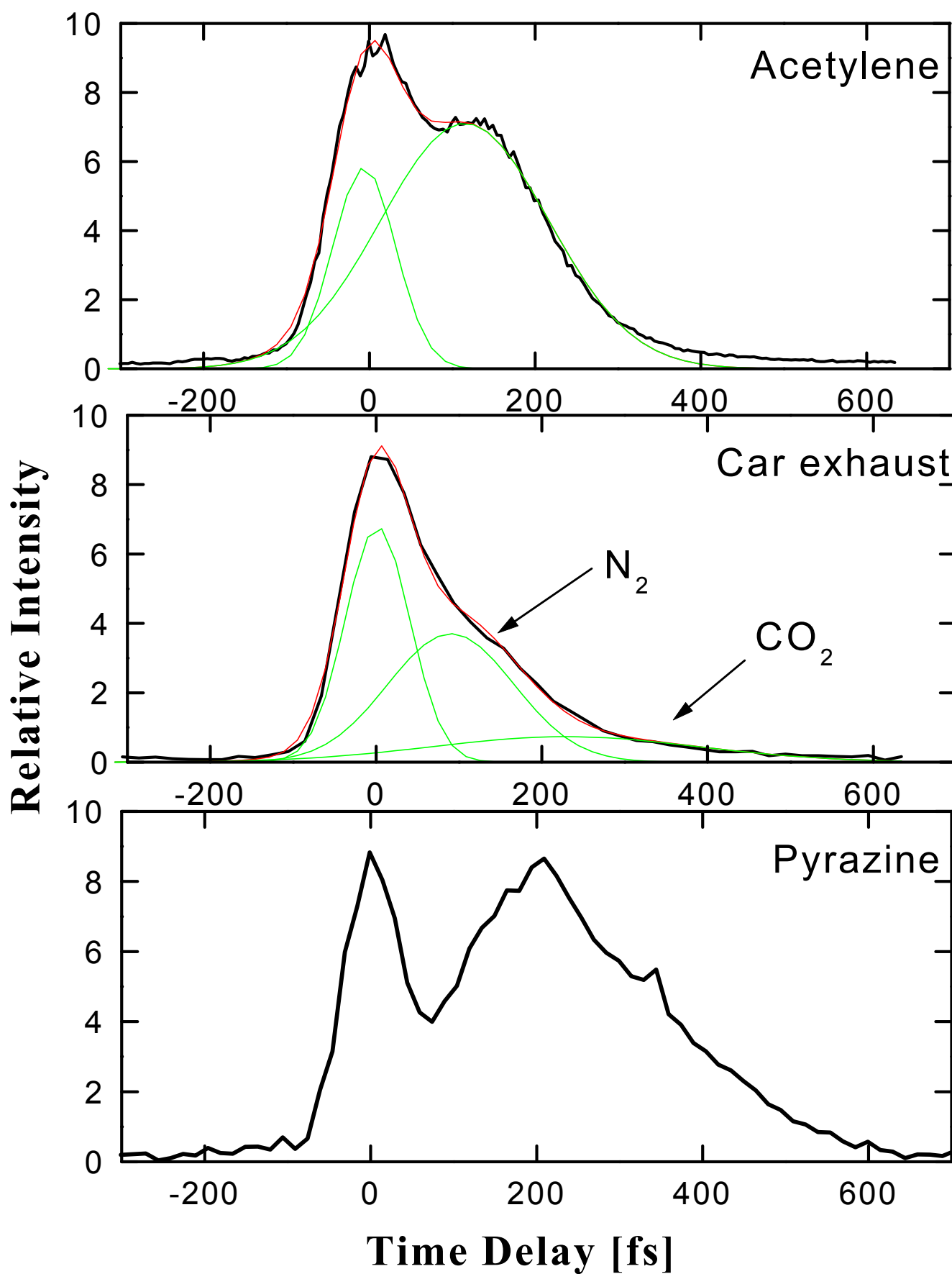


Fig. 8; Dantus, Femtochemistry

